Modeling and Analysis of a Strongly Coupled Series–Parallel-Compensated Wireless Power Transfer System

Yiming Zhang, *Member, IEEE*, Zhengchao Yan, *Student Member, IEEE*, Tianze Kan, *Student Member, IEEE*, Xiaosheng Zeng, Shuangquan Chen, and Chunting Chris Mi, *Fellow, IEEE*

***Abstract*— In the wireless charging of high-power electric buses or low-power consumer electronics, the charging distance is normally very small, leading to a strong coupling. Current distortion occurs for a wireless power transfer (WPT) system with a strong coupling. This paper investigates the strongly coupled series–parallel (SP)-compensated WPT system, where the first harmonic approximation (FHA) is no longer valid. A mathematical model of an SP-compensated WPT system based on differential equations is built. There are two sinusoidal components with significantly different frequencies existing in the transmitter and receiver currents, which cause the current distortion. The proposed model and FHA are compared, and the proposed model is more accurate than FHA. The estimations of the current root-mean-square values from FHA tend to be smaller than those from the proposed model and the measured values. In addition, it is found that with the increasing rectifier dc current, the system transits from zero voltage switching to zero current switching. The critical rectifier dc current decreases with the increasing operating frequency. The experimental results verify the effectiveness of the proposed model. The proposed model promotes a better design of an SP-compensated strongly coupled WPT system.**

***Index Terms*— Differential equations (DEs), distortion, modeling, series–parallel (SP) compensation, wireless power transfer (WPT), zero current switching (ZCS), zero voltage switching (ZVS).**

I. Introduction

WIRELESS power transfer (WPT) technology has currently undergone booming development [1]–[3]. The most common WPT technology is inductive power transfer (IPT) based on magnetic induction. In IPT, the alternating magnetic flux generated by the transmitter (TX) is linked to the receiver (RX) and results in an induced voltage on the RX. Power will be transferred to the load when connected to the RX.

The compensation, or matching network, is crucial in IPT in that capacitors and inductors are utilized to improve efficiency and reduce the voltampere rating by adjusting the reactive power [4]. Basically, there are two compensation topologies, the series (S) compensation and the parallel (P) compensation. The inductor can be regarded as a current source and the capacitor as a voltage source. Because two current sources cannot be connected in series and two voltage sources cannot be connected in parallel, the S compensation should be connected to a voltage source and the P compensation should be connected to a current source. Due to the easier energy storage in the capacitor than that in the inductor, the voltage-source inverter (VSI) is overwhelmingly utilized as the source in a WPT system compared with the current-source inverter [5]. While the S compensation can be directly connected to the VSI, an extra inductor should be inserted between the VSI and the P compensation, forming an inductor–capacitor–inductor (LCL) compensation [6]. By inserting a capacitor in the branch of the transmission coil in the LCL compensation, the inductor–capacitor–capacitor (LCC) compensation is formed and it is more popular than the LCL compensation due to an additional degree of freedom for designing a WPT system [7].

When the VSI is employed on the TX side, there are six compensation topologies, namely, SS, series–parallel (SP), S-LCC, LCC-S, LCC-P, and LCC–LCC, shown in Fig. 1. This paper deals with SP topology.

For the SP topology, the VSI and the current-source rectifier are adopted [8]. The TX voltage and the RX current are

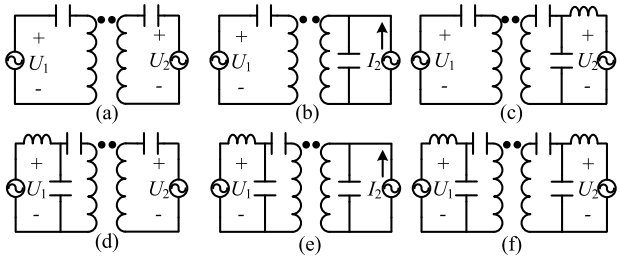

Fig. 1. Compensation Topologies. (a) SS. (b) SP. (c) S-LCC. (d) LCC-S. (e) LCC-P. (f) LCC–LCC.

Manuscript received February 28, 2018; revised May 1, 2018; accepted July 21, 2018. Date of publication July 27, 2018; date of current version May 1, 2019. This work was supported by Huawei Technologies Co., Ltd., under Grant 9406139. Recommended for publication by Associate Editor Chi K. Lee. *(Corresponding author: Chunting Chris Mi.)*

Y. Zhang, T. Kan, and C. Mi are with the Department of Electrical and Computer Engineering, San Diego State University, San Diego, CA 92182 USA (e-mail: mi@ieee.org).

Z. Yan is with the Department of Electrical and Computer Engineering, San Diego State University, San Diego, CA 92182 USA, and also with the School of Marine Science and Technology, Northwestern Polytechnical University, Xi'an 710072, China.

X. Zeng and S. Chen are with Huawei Technologies Co., Ltd., Shenzhen 518000, China.

Color versions of one or more of the figures in this paper are available online at http://ieeexplore.ieee.org.

Digital Object Identifier 10.1109/JESTPE.2018.2860935

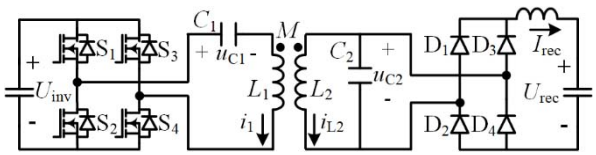

Fig. 2. Topology of SP compensation.

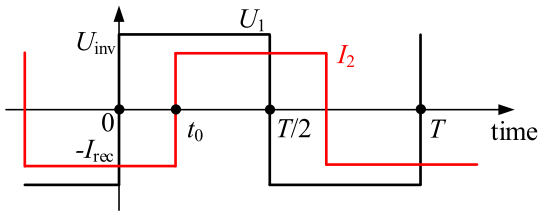

Fig. 3. Waveforms of ac voltage of the inverter and ac current of the rectifier.

square waves. Based on first harmonic approximation (FHA), only their fundamental components are considered [9]–[12]. In most cases, it is accurate due to the frequency selection characteristic of the resonant circuit where high-order harmonics are suppressed. However, it has been found that with a strong coupling, the current waveforms of the WPT system with the SP compensation are distorted and the harmonics are not negligible, leading to inaccuracy of FHA. The application scenarios of WPT systems with a strong coupling include: 1) wireless charging for electric buses where the charging distance can be smaller than 50 mm [13] and 2) wireless charging for consumer electronics where the receiving coil is attached to the surface of the transmitting coil to form a large coupling. A typical example is Conductix-Wampfler which achieved 60-kW power transfer at a distance of 40 mm [14].

In this paper, the model of an SP-compensated WPT system is built based on differential equations (DEs). The comparison between the proposed model and FHA is conducted, and the soft switching status is studied. An experimental prototype is implemented to validate the analysis.

II. Modeling and Derivation

A. SP Compensation

The topology of an SP-compensated WPT system is depicted in Fig. 2, where S_1–S_4 are the full-controlled semiconductor switches of the inverter, D_1–D_4 are the diodes of the rectifier, R_1 (R_2), L_1 (L_2), C_1 (C_2), i_1 (i_{L2}), and u_{C1} (u_{C2}) are the equivalent resistance, the inductance, the compensating capacitance, the coil current, and the capacitor voltage of the TX (RX), respectively, M is the mutual inductance, U_{inv} and U_1 are the inverter dc and ac voltages, respectively, and I_{rec} and I_2 are the rectifier dc and ac currents, respectively.

Assuming the TX and RX resonate at the same resonant angular frequency ω_0, we have

$$\omega_0 = \frac{1}{\sqrt{L_1C_1}} = \frac{1}{\sqrt{L_2C_2}}. \tag{1}$$

Define

$$L_0 = \sqrt{L_1L_2},\ \lambda = \sqrt{\frac{L_1}{L_2}}. \tag{2}$$

Thus

$$M = kL_0,\ \ L_1 = \lambda L_0,\ \ L_2 = \frac{L_0}{\lambda},\ C_1 = \frac{1}{\omega_0^2\lambda L_0},\ \ C_2 = \frac{\lambda}{\omega_0^2 L_0} \tag{3}$$

where k is the coupling coefficient.

The model of an SP-compensated WPT system based on FHA can be found in [12]. However, FHA is not accurate, especially when the coupling gets strong. In this paper, the model of the SP-compensated WPT system will be built based on DEs.

The operating angular frequency, which can be different from the resonant frequency, is denoted as ω. The corresponding cycle is indicated as T. The waveforms of U_1 and I_2 are shown in Fig. 3. Since the waveforms are half-wave symmetrical, only the first half cycle is analyzed. The results of the first half cycle can be easily extended to the second half cycle. t_0 is the zero crossing point of the rectifier, where u_{C2} changes from negative to positive. During the stage [0, t_0], S_1, S_4, D_2, and D_3 are ON and the other switches are OFF; during the stage [t_0, $T/2$], S_1, S_4, D_1, and D_4 are ON and the other switches are OFF.

Take the inductor currents and the capacitor voltages i_1, i_{L2}, u_{C1}, and u_{C2} as the state variables, and the model in Fig. 2 for the stage [0, t_0] can be established by

$$\begin{cases} U_{\text{inv}} = u_{C1} + \lambda L_0\dfrac{di_1}{dt} + kL_0\dfrac{di_{L2}}{dt}, \quad i_1 = \dfrac{1}{\omega_0^2\lambda L_0}\dfrac{du_{C1}}{dt} \\ -I_{\text{rec}} = i_{L2} + \dfrac{\lambda}{\omega_0^2 L_0}\dfrac{du_{C2}}{dt}, \quad u_{C2} = \dfrac{L_0}{\lambda}\dfrac{di_{L2}}{dt} + kL_0\dfrac{di_1}{dt}. \end{cases} \tag{4}$$

Regard $\lambda \cdot i_1$ and $\lambda \cdot u_{C2}$ in (4) as new variables i_1 and u_{C2}, and (4) can be transformed into the case with symmetrical TX and RX, given as

$$\begin{cases} U_{\text{inv}} = u_{C1} + L_0\dfrac{di_1}{dt} + kL_0\dfrac{di_{L2}}{dt}, \quad i_1 = \dfrac{1}{\omega_0^2 L_0}\dfrac{du_{C1}}{dt} \\ -I_{\text{rec}} = i_{L2} + \dfrac{1}{\omega_0^2 L_0}\dfrac{du_{C2}}{dt}, \quad u_{C2} = L_0\dfrac{di_{L2}}{dt} + kL_0\dfrac{di_1}{dt}. \end{cases} \tag{5}$$

This paper mainly deals with the case with a symmetrical structure. By solving (5), the DEs for the inductor currents can be expressed by

$$\begin{cases} \dfrac{1+k}{\omega_0^2}\dfrac{d^2(i_1+i_{L2})}{dt^2} + (i_1+i_{L2}) = -I_{\text{rec}} \\ \dfrac{1-k}{\omega_0^2}\dfrac{d^2(i_1-i_{L2})}{dt^2} + (i_1-i_{L2}) = I_{\text{rec}}. \end{cases} \tag{6}$$

The characteristic roots for (6) can be given as

$$\omega_P = \frac{\omega_0}{\sqrt{1+k}}, \quad \omega_N = \frac{\omega_0}{\sqrt{1-k}}. \tag{7}$$

The state variables in the stage $[0,\ t_0]$ can be expressed as

$$\begin{cases} i_{1-1} = \dfrac{A_{1P}}{2}\sin(\omega_P t + B_{1P}) + \dfrac{A_{1N}}{2}\sin(\omega_N t + B_{1N}) \\ i_{L2-1} = -I_{\text{rec}} - \dfrac{A_{1P}}{2}\sin(\omega_P t + B_{1P}) + \dfrac{A_{1N}}{2}\sin(\omega_N t + B_{1N}) \\ u_{C1-1} = U_{\text{inv}} - \dfrac{(1+k)\omega_P L_0}{2}A_{1P}\cos(\omega_P t + B_{1P}) \\ \qquad\quad - \dfrac{(1-k)\omega_N L_0}{2}A_{1N}\sin(\omega_N t + B_{1N}) \\ u_{C2-1} = \dfrac{(1+k)\omega_P L_0}{2}A_{1P}\cos(\omega_P t + B_{1P}) \\ \qquad\quad - \dfrac{(1-k)\omega_N L_0}{2}A_{1N}\sin(\omega_N t + B_{1N}) \end{cases} \tag{8}$$

where A_{1P}, A_{1N}, B_{1P}, and B_{1N} are the coefficients to be determined.

Similarly, the model in Fig. 2 for the stage $[t_0,\ T/2]$ can be established by

$$\begin{cases} U_{\text{inv}} = u_{C1} + L_0\dfrac{di_1}{dt} + kL_0\dfrac{di_{L2}}{dt}, \quad i_1 = \dfrac{1}{\omega_0^2 L_0}\dfrac{du_{C1}}{dt} \\ I_{\text{rec}} = i_{L2} + \dfrac{1}{\omega_0^2 L_0}\dfrac{du_{C2}}{dt}, \quad u_{C2} = L_0\dfrac{di_{L2}}{dt} + kL_0\dfrac{di_1}{dt}. \end{cases} \tag{9}$$

The DEs and the characteristic roots are the same as those of the first stage shown in (6) and (7). The state variables of stage $[t_0,\ T/2]$ can be expressed as

$$\begin{cases} i_{1-2} = \dfrac{A_{2P}}{2}\sin(\omega_P t + B_{2P}) + \dfrac{A_{2N}}{2}\sin(\omega_N t + B_{2N}) \\ i_{L2-2} = I_{\text{rec}} + \dfrac{A_{2P}}{2}\sin(\omega_P t + B_{2P}) - \dfrac{A_{2N}}{2}\sin(\omega_N t + B_{2N}) \\ u_{C1-2} = U_{\text{inv}} - \dfrac{(1+k)\omega_P L_0}{2}A_{2P}\cos(\omega_P t + B_{2P}) \\ \qquad\quad - \dfrac{(1-k)\omega_N L_0}{2}A_{2N}\sin(\omega_N t + B_{2N}) \\ u_{C2-2} = \dfrac{(1+k)\omega_P L_0}{2}A_{2P}\cos(\omega_P t + B_{2P}) \\ \qquad\quad - \dfrac{(1-k)\omega_N L_0}{2}A_{2N}\sin(\omega_N t + B_{2N}) \end{cases} \tag{10}$$

where A_{2P}, A_{2N}, B_{2P}, and B_{2N} are the coefficients to be determined.

To calculate the coefficients in (8) and (10), the initial conditions are

$$\begin{cases} u_{C2-1}(t_0) = 0,\ i_{1-1}(0) = -i_{1-2}\left(\dfrac{T}{2}\right),\ i_{1-1}(t_0) = i_{1-2}(t_0) \\ i_{L2-1}(0) = -i_{L2-2}\left(\dfrac{T}{2}\right), \quad i_{L2-1}(t_0) = i_{L2-2}(t_0) \\ u_{C1-1}(0) = -u_{C1-2}\left(\dfrac{T}{2}\right), \quad u_{C1-1}(t_0) = u_{C1-2}(t_0) \\ u_{C2-1}(0) = -u_{C2-2}\left(\dfrac{T}{2}\right), \quad u_{C2-1}(t_0) = u_{C2-2}(t_0). \end{cases} \tag{11}$$

Solving (11) yields

$$\begin{cases} A_{1P}\sin B_{1P} = \dfrac{\cos\omega_P\left(t_0 - \frac{T}{2}\right) + \cos\omega_P t_0}{1 + \cos\frac{\omega_P T}{2}} I_{\text{rec}} \\ \qquad\quad - \dfrac{\sin\frac{\omega_P T}{2}}{1 + \cos\frac{\omega_P T}{2}} \dfrac{U_{\text{inv}}}{(1+k)\omega_P L_0} \\ A_{1P}\cos B_{1P} = \dfrac{\sin\omega_P\left(t_0 - \frac{T}{2}\right) + \sin\omega_P t_0}{1 + \cos\frac{\omega_P T}{2}} I_{\text{rec}} \\ \qquad\quad + \dfrac{U_{\text{inv}}}{(1+k)\omega_P L_0} \\ A_{1N}\sin B_{1N} = -\dfrac{\cos\omega_N\left(t_0 - \frac{T}{2}\right) + \cos\omega_N t_0}{1 + \cos\frac{\omega_N T}{2}} I_{\text{rec}} \\ \qquad\quad - \dfrac{\sin\frac{\omega_N T}{2}}{1 + \cos\frac{\omega_N T}{2}} \dfrac{U_{\text{inv}}}{(1-k)\omega_N L_0} \\ A_{1N}\cos B_{1N} = -\dfrac{\sin\omega_N(t_0 - \frac{T}{2}) + \sin\omega_N t_0}{1 + \cos\frac{\omega_N T}{2}} I_{\text{rec}} \\ \qquad\quad + \dfrac{U_{\text{inv}}}{(1-k)\omega_N L_0} \\ A_{2P}\sin B_{2P} = -\dfrac{\cos\omega_P\left(t_0 + \frac{T}{2}\right) + \cos\omega_P t_0}{1 + \cos\frac{\omega_P T}{2}} I_{\text{rec}} \\ \qquad\quad - \dfrac{\sin\frac{\omega_P T}{2}}{1 + \cos\frac{\omega_P T}{2}} \dfrac{U_{\text{inv}}}{(1+k)\,\omega_P L_0} \\ A_{2P}\cos B_{2P} = -\dfrac{\sin\omega_P\left(t_0 + \frac{T}{2}\right) + \sin\omega_P t_0}{1 + \cos\frac{\omega_P T}{2}} I_{\text{rec}} \\ \qquad\quad + \dfrac{U_{\text{inv}}}{(1+k)\omega_P L_0} \\ A_{2N}\sin B_{2N} = \dfrac{\cos\omega_N\left(t_0 + \frac{T}{2}\right) + \cos\omega_N t_0}{1 + \cos\frac{\omega_N T}{2}} I_{\text{rec}} \\ \qquad\quad - \dfrac{\sin\frac{\omega_N T}{2}}{1 + \cos\frac{\omega_N T}{2}} \dfrac{U_{\text{inv}}}{(1-k)\omega_N L_0} \\ A_{2N}\cos B_{2N} = \dfrac{\sin\omega_N\left(t_0 + \frac{T}{2}\right) + \sin\omega_N t_0}{1 + \cos\frac{\omega_N T}{2}} I_{\text{rec}} \\ \qquad\quad + \dfrac{U_{\text{inv}}}{(1-k)\omega_N L_0}. \end{cases} \tag{12}$$

where t_0 in is an unknown variable and can be calculated from $u_{C2-1}(t_0) = 0$ in (11), which can be transformed into

$$\begin{aligned} &\left[\sqrt{1+k}\tan\left(\frac{\omega_0}{\omega}\frac{\pi}{2\sqrt{1+k}}\right) + \sqrt{1-k}\tan\left(\frac{\omega_0}{\omega}\frac{\pi}{2\sqrt{1-k}}\right)\right] \\ &\quad\times\frac{\omega_0 L_0 I_{\text{rec}}}{U_{\text{inv}}} = \frac{\cos\left(\frac{\omega_0 t_0}{\sqrt{1+k}} - \frac{\omega_0}{\omega}\frac{\pi}{2\sqrt{1+k}}\right)}{\cos\left(\frac{\omega_0}{\omega}\frac{\pi}{2\sqrt{1+k}}\right)} \\ &\qquad - \frac{\cos\left(\frac{\omega_0 t_0}{\sqrt{1-k}} - \frac{\omega_0}{\omega}\frac{\pi}{2\sqrt{1-k}}\right)}{\cos\left(\frac{\omega_0}{\omega}\frac{\pi}{2\sqrt{1-k}}\right)}. \end{aligned} \tag{13}$$

Thus, the equations for the inductor currents and the capacitor voltages can be obtained.

We can see from (8) and (10) that the TX and RX currents are composed of two different sinusoidal components, whose frequencies are related to the two characteristic frequencies shown in (7). These two characteristic frequencies varying

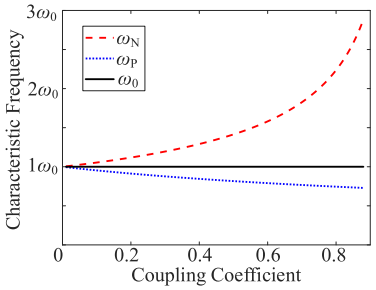

Fig. 4. Characteristic frequencies varying with coupling coefficient.

with the coupling coefficient are plotted in Fig. 4. When the coupling coefficient is small, these two characteristic frequencies are close to each other. With the increasing coupling coefficient, the difference between these two frequencies is becoming more and more significant. It is the composition of these two distinctively different frequency components that leads to distortion.

In Fig. 3, at time 0, the sign of the TX coil current determines the soft switching of the inverter. When the TX coil current is larger than 0, zero current switching (ZCS) is achieved; when smaller than 0, zero voltage switching (ZVS) is achieved. Combined with (13), the TX coil current at time 0 can be expressed as

$$\begin{aligned} & i_{1-1}(0) \\ &= \left[\sqrt{1+k}\tan\left(\frac{\omega_0}{\omega}\frac{\pi}{2\sqrt{1+k}}\right)+\sqrt{1-k}\tan\left(\frac{\omega_0}{\omega}\frac{\pi}{2\sqrt{1-k}}\right)\right] \\ &\quad\times\frac{\omega_0 L_0 I_{\text{rec}}^2}{2U_{\text{inv}}}-\left[\frac{\tan\left(\frac{\omega_0}{\omega}\frac{\pi}{2\sqrt{1+k}}\right)}{\sqrt{1+k}}+\frac{\tan\left(\frac{\omega_0}{\omega}\frac{\pi}{2\sqrt{1-k}}\right)}{\sqrt{1-k}}\right]\frac{U_{\text{inv}}}{2\omega_0 L_0}. \end{aligned} \tag{14}$$

The critical I_{rec} to achieve zero phase angle can be expressed as

$$\begin{aligned} I_{\text{rec-crt}} &= \frac{U_{\text{inv}}}{\omega_0 L_0} \\ &\quad\times\frac{\frac{\tan\left(\frac{\omega_0}{\omega}\frac{\pi}{2\sqrt{1+k}}\right)}{\sqrt{1+k}}+\frac{\tan\left(\frac{\omega_0}{\omega}\frac{\pi}{2\sqrt{1-k}}\right)}{\sqrt{1-k}}}{\sqrt{1+k}\tan\left(\frac{\omega_0}{\omega}\frac{\pi}{2\sqrt{1+k}}\right)+\sqrt{1-k}\tan\left(\frac{\omega_0}{\omega}\frac{\pi}{2\sqrt{1-k}}\right)}. \end{aligned} \tag{15}$$

When the rectifier dc current is larger than this critical value, the TX coil current is larger than 0 at time 0, achieving ZCS; when smaller, the TX coil current is smaller than 0 at time 0, achieving ZVS. There are two factors that impact the critical rectifier dc current: operating angular frequency ω and coupling coefficient k. Assume that the fiducial value for the critical rectifier dc current is $U_{\text{inv}}/(\omega_0 L_0)$. The relationship between the per-unit value of the critical rectifier dc current and the coupling coefficient at the resonant angular frequency ω_0 is depicted in Fig. 5. The critical rectifier dc current increases with the increasing coupling coefficient in this case.

B. Other Compensations

The above approach can be applied to other compensation topologies, for example, the SS compensation shown in Fig. 6.

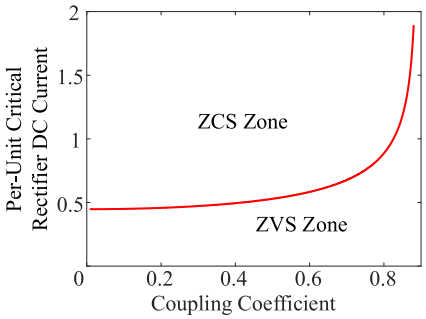

Fig. 5. Critical rectifier dc current to divide ZVS and ZCS zones.

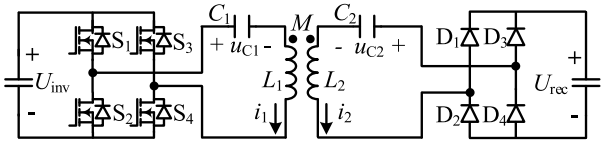

Fig. 6. Topology of SS compensation.

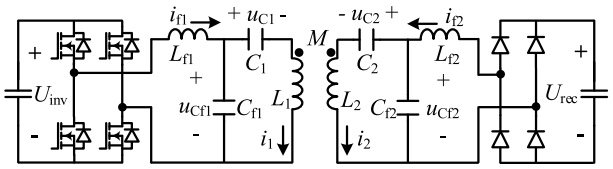

Fig. 7. Topology of LCC–LCC compensation.

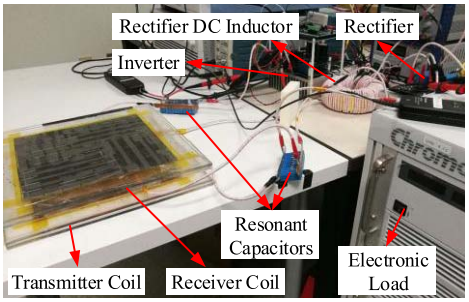

Fig. 8. Photograph of experimental prototype.

For the ease of analysis, assume that $L_1 = L_2 = L_0$ and $C_1 = C_2 = C_0$. Thus, $M = k \cdot L_0$. Take the inductor currents and capacitor voltages i_1, i_2, u_{C1}, and u_{C2} as the state variables, when U_{inv} and U_{rec} are positively connected to the circuit, we have

$$\begin{cases} U_{\text{bus}} = u_{C1} + L_0\dfrac{di_1}{dt} + kL_0\dfrac{di_2}{dt}, \quad i_1 = C_0\dfrac{du_{C1}}{dt} \\ U_{\text{bat}} = u_{C2} + L_0\dfrac{di_2}{dt} + kL_0\dfrac{di_1}{dt}, \quad i_2 = C_0\dfrac{du_{C2}}{dt}. \end{cases} \tag{16}$$

By solving (16), the DEs for the inductor currents can be expressed as

$$\begin{cases} \dfrac{1+k}{\omega_0^2}\dfrac{d^2(i_1+i_2)}{dt^2} + (i_1+i_2) = 0 \\ \dfrac{1-k}{\omega_0^2}\dfrac{d^2(i_1-i_2)}{dt^2} + (i_1-i_2) = 0. \end{cases} \tag{17}$$

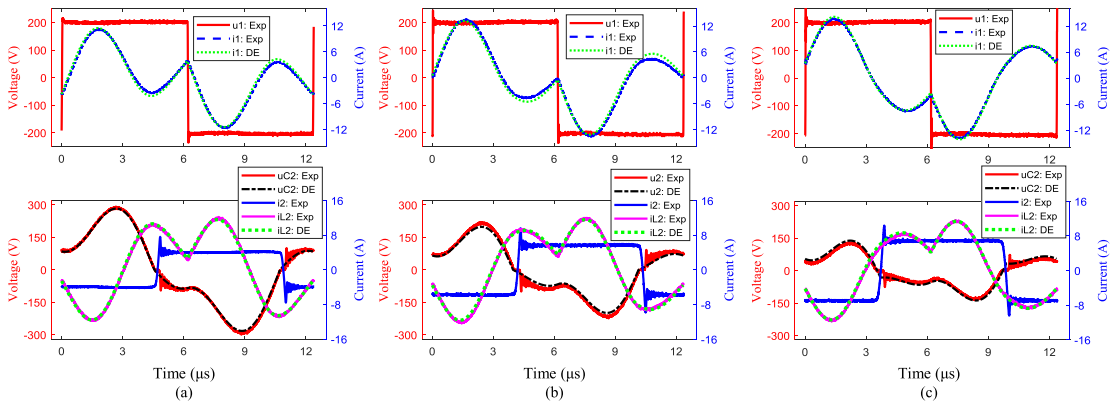

Fig. 9. Voltage and current waveforms. (a) $I_{\text{rec}} = 3.952$ A. (b) $I_{\text{rec}} = 5.655$ A. (c) $I_{\text{rec}} = 6.868$ A.

Comparing (17) and (6), we can see that the SP and SS compensations have the same DEs. Hence, they have the same characteristic roots. Similar derivation process can be obtained for the SS compensation.

Another example is the LCC–LCC compensation topology shown in Fig. 7, where L_{f1} (L_{f2}), C_{f1} (C_{f2}), i_{f1} (i_{f2}), and u_{Cf1} (u_{Cf2}) are the TX (RX) compensation inductor, the compensation capacitor, the inductor current, and the capacitor voltage.

Similarly, assume that $L_1 = L_2 = L_0$, $C_1 = C_2 = C_0$, $L_{f1} = L_{f2} = L_{f0}$, and $C_{f1} = C_{f2} = C_{f0}$. Thus, $M = k \cdot L_0$. Define $\alpha = L_{f0}/L_0$. Take the inductor currents and capacitor voltages i_1, i_2, i_{f1}, i_{f2}, u_{C1}, u_{C2}, u_{Cf1}, and u_{Cf2} as the state variables, when U_{inv} and U_{rec} are positively connected to the circuit, we have

$$\begin{cases} U_{\text{bus}} = L_{f0}\dfrac{di_{f1}}{dt} + u_{Cf1}, & -U_{\text{bat}} = L_{f0}\dfrac{di_{f2}}{dt} + u_{Cf2} \\ i_{f1} = C_{f0}\dfrac{du_{Cf1}}{dt} + i_1, & i_{f2} = C_{f0}\dfrac{du_{Cf2}}{dt} + i_2 \\ u_{Cf1} = u_{C1} + L_0\dfrac{di_1}{dt} + kL_0\dfrac{di_2}{dt}, & i_1 = C_0\dfrac{du_{C1}}{dt} \\ u_{Cf2} = u_{C2} + L_0\dfrac{di_2}{dt} + kL_0\dfrac{di_1}{dt}, & i_2 = C_0\dfrac{du_{C2}}{dt}. \end{cases} \tag{18}$$

The DEs for i_1 and i_2 can be derived as

$$\begin{cases} \dfrac{1+k}{\omega_0^4(1-\alpha)}\dfrac{d^4(i_1+i_2)}{dt^4} \\ \qquad + \dfrac{2+k}{\omega_0^2(1-\alpha)}\dfrac{d^2(i_1+i_2)}{dt^2} + (i_1+i_2) = 0 \\ \dfrac{1-k}{\omega_0^4(1-\alpha)}\dfrac{d^4(i_1-i_2)}{dt^4} \\ \qquad + \dfrac{2-k}{\omega_0^2(1-\alpha)}\dfrac{d^2(i_1-i_2)}{dt^2} + (i_1-i_2) = 0. \end{cases} \tag{19}$$

Since the number of passive elements in the LCC–LCC compensations doubles that of the SP and SS compensation, the order of the DEs also doubles. However, similar derivation process can still be obtained for the LCC–LCC compensation.

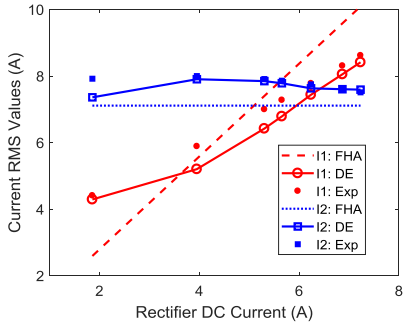

Fig. 10. Root-mean-square values of TX and RX currents.

III. Calculations and Experiments

An experimental prototype of the WPT system with the SP compensation is implemented, shown in Fig. 8. The parameters of the TX and RX coils are the same. $L_0 = 62.5$ μH, $C_0 = 62$ nF, and $k = 0.796$. Thus, the resonant frequency is 81 kHz. The rectifier dc inductor is 713 μH, which is large enough to have a stable dc rectifier current.

When $U_{\text{inv}} = 200$ V, the voltage and current waveforms under different rectifier dc currents at the resonant frequency are plotted in Fig. 9. With a strong coupling, the TX and RX coil currents are distorted and FHA is no longer effective. The proposed model, which is based on the DEs, agrees well with the measurements.

The rms values of the TX and RX coil currents varying with the rectifier dc current are shown in Fig. 10. The TX coil current increases with the increasing rectifier dc current, but not exactly as estimated by FHA. The RX coil current remains approximately the same with the increasing rectifier dc current, but larger than the calculations from FHA. The proposed model matches better with the experimental results than FHA.

As can be seen from Fig. 9, with the increasing rectifier dc current, the TX coil current at time 0 changes from negative to positive, indicating that the operating state of the system transitions from ZVS to ZCS. The critical rectifier dc current when the TX coil current is 0 at time 0 can be calculated from (15). At the coupling coefficient of 0.796, the calculations and the experimental results of the critical rectifier dc current

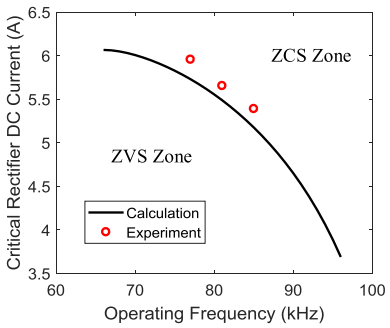

Fig. 11. Critical rectifier dc current varying with operating frequency.

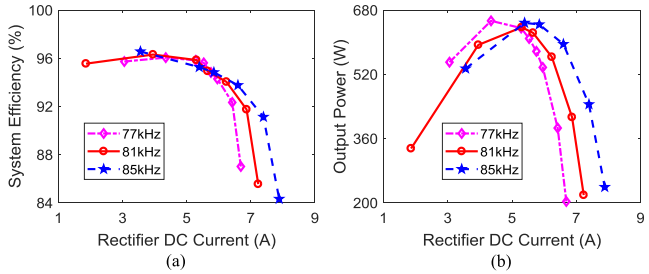

Fig. 12. Experimental results versus rectifier dc current. (a) System efficiency. (b) Output power.

varying with the operating frequency are depicted in Fig. 11. The critical rectifier dc current decreases with the increasing operating frequency. Therefore, the operating frequency can be adjusted to alter the WPT system operated in a ZVS or a ZCS state.

When $U_{\text{inv}} = 200$ V, the system efficiency and the output power varying with the rectifier dc current under different operating frequencies are shown in Fig. 12. With a wide variation of the operating frequency, the system efficiency and the output power remain stable. In addition, there is a maximum output power corresponding to a particular rectifier dc current. This particular rectifier dc current to achieve the maximum output power is close to the value of 5.6 A derived in [12], expressed as

$$I_{\text{rec}-\max P} = \frac{\sqrt{2}}{2}\frac{U_{\text{inv}}}{\omega M}. \tag{20}$$

Below this rectifier dc current value, the output power is proportional to the rectifier dc current. Also, the WPT system works in the ZVS zone, which is good for the efficiency of the inverter where metal–oxide–semiconductor field effect transistors are adopted. Hence, the system efficiency remains high in this area.

IV. Conclusion

The model of an SP-compensated WPT system has been established based on DEs. The analytical expressions of the coil currents and capacitor voltages have been derived. There are two sinusoidal components with frequencies related to the coupling coefficient in the TX and RX coil currents. Under a strong coupling, these two frequencies are significantly different, resulting in the current distortion. Thus, compared with FHA, the proposed model achieves more accurate results. Furthermore, it has been found that with the increasing rectifier dc current, the system transits from ZVS to ZCS. The critical rectifier dc current decreases with the increasing operating frequency. The system achieves stable high system efficiency and output power. Therefore, the operating frequency can be adjusted to achieve ZVS or ZCS. An experimental prototype has been implemented. The proposed model matches well with the experimental results.

The DEs for the SS and LCC–LCC compensations have also been derived which shows that the proposed model can be easily applied to other compensations. With the proposed model, this paper tries to offer insight into the distortion mechanism and practical design of a strongly coupled SP-compensated WPT system, and also for other compensations.

References

[1] C. C. Mi, G. Buja, S. Y. Choi, and C. T. Rim, "Modern advances in wireless power transfer systems for roadway powered electric vehicles," *IEEE Trans. Ind. Electron.*, vol. 63, no. 10, pp. 6533–6545, Oct. 2016.

[2] Z. Li, C. Zhu, J. Jiang, K. Song, and G. Wei, "A 3-kW wireless power transfer system for sightseeing car supercapacitor charge," *IEEE Trans. Power Electron.*, vol. 32, no. 5, pp. 3301–3316, May 2017.

[3] Z. Zhang, K. T. Chau, C. Qiu, and C. Liu, "Energy encryption for wireless power transfer," *IEEE Trans. Power Electron.*, vol. 30, no. 9, pp. 5237–5246, Sep. 2015.

[4] W. Zhang and C. C. Mi, "Compensation topologies of high-power wireless power transfer systems," *IEEE Trans. Veh. Technol.*, vol. 65, no. 6, pp. 4768–4778, Jun. 2016.

[5] Y. Zhang, K. Chen, F. He, Z. Zhao, T. Lu, and L. Yuan, "Closed-form oriented modeling and analysis of wireless power transfer system with constant-voltage source and load," *IEEE Trans. Power Electron.*, vol. 31, no. 5, pp. 3472–3481, May 2015.

[6] D. Xin *et al.*, "Improved LCL resonant network for inductive power transfer system," in *Proc. IEEE PELS Workshop Emerg. Technol., Wireless Power (WoW)*, Jun. 2015, pp. 1–5.

[7] T. Kan, T.-D. Nguyen, J. C. White, R. K. Malhan, and C. C. Mi, "A new integration method for an electric vehicle wireless charging system using LCC compensation topology: Analysis and design," *IEEE Trans. Power Electron.*, vol. 32, no. 2, pp. 1638–1650, Feb. 2017.

[8] R. Bosshard, J. W. Kolar, J. Muhlethaler, I. Stevanovic, B. Wunsch, and F. Canales, "Modeling and η-α-Pareto optimization of inductive power transfer coils for electric vehicles," *IEEE J. Emerg. Sel. Topics Power Electron.*, vol. 3, no. 1, pp. 50–64, Mar. 2015.

[9] H. Liu, Q. Chen, G. Ke, X. Ren, and S.-C. Wong, "Research of the input-parallel output-series inductive power transfer system," in *Proc. IEEE PELS Workshop Emerg. Technol., Wireless Power (WoW)*, Jun. 2015, pp. 1–7.

[10] Y.-H. Chao, J.-J. Shieh, C.-T. Pan, and W.-C. Shen, "A closed-form oriented compensator analysis for series-parallel loosely coupled inductive power transfer systems," in *Proc. IEEE Power Electron. Spec. Conf. (PESC)*, Jun. 2007, pp. 1215–1220.

[11] H. H. Wu, G. A. Covic, J. T. Boys, and A. P. Hu, "A 1 kW inductive charging system using AC processing pickups," in *Proc. IEEE Conf. Ind. Electron. Appl. (ICIEA)*, Jun. 2011, pp. 1999–2004.

[12] Y. Zhang, Z. Zhao, and Y. Jiang, "Modeling and analysis of wireless power transfer system with constant-voltage source and constant-current load," in *Proc. IEEE Energy Convers. Congr. Expo. (ECCE)*, Oct. 2017, pp. 975–979.

[13] Z. Bi, T. Kan, C. C. Mi, Y. Zhang, Z. Zhao, and G. A. Keoleian, "A review of wireless power transfer for electric vehicles: Prospects to enhance sustainable mobility," *Appl. Energy*, vol. 179, pp. 413–425, Oct. 2016.

[14] Conductix-Wampfler. (2013). *Charging Electric Buses Quickly and Efficiently: Bus Stops Fitted With Modular Components Make 'Charge & Go,' Simple to Implement.* [Online]. Available: http://www.conductix.us/en/news/2013-05-29/charging-electric-buses-quickly-and-efficiently-bus-stops-fitted-modular-components-make-charge-go

Yiming Zhang (S'13–M'16) received the B.S. and Ph.D. degrees in electrical engineering from Tsinghua University, Beijing, China, in 2011 and 2016, respectively.

He is currently a Post-Doctoral Researcher with San Diego State University, San Diego, CA, USA. His current research interests include wireless power transfer for electric vehicles and mobile phones, and resonant converters.

Zhengchao Yan (S'18) received the B.S. degree in mechanical design, manufacturing and automation from Northwestern Polytechnical University, Xi'an, China, in 2013, where he is currently pursuing the Ph.D. degree.

In 2017, he received the funding from the China Scholarship Council, and became a joint Ph.D. student in the Department of Electrical and Computer Engineering, San Diego State University, San Diego, CA, USA. His current research interests include wireless power transfer, including coil design and compensation topologies.

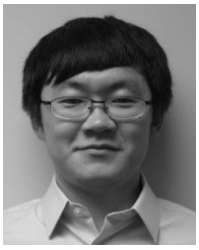

Tianze Kan (S'15) received the B.Eng. degree in electrical engineering and automation from the Huazhong University of Science and Technology, Wuhan, China, in 2011, and the M.S. degree in electrical engineering from the University of Southern California, Los Angeles, CA, USA, in 2013. He is currently pursuing the Ph.D. degree in electrical and computer engineering in the joint doctoral program between San Diego State University, San Diego, CA, USA, and the University of California San Diego, La Jolla, CA, USA.

His current research interests include power electronics and inductive-based wireless power transfer, especially on coil design and compensation topologies.

Xiaosheng Zeng received the B.S. degree in electronic engineering from Sun Yat-sen University, Guangzhou, China, in 2009, and the M.S. degree in power electronics from the South China University of Technology, Guangzhou, in 2012.

In 2012, he joined Huawei Technologies Co., Ltd., Shenzhen, China, where he is currently a Researcher with the Department of Central Research Institute. His current research interests include wireless power transfer, power electronics, and battery management.

Shuangquan Chen was born in Hunan, China, in 1985.He received the B.S. degree from the Harbin Institute of Technology, Weihai, China, in 2008, and the M.S. degree from the Shenzhen Graduate School, Harbin Institute of Technology Shenzhen, China, in 2011.

His current research interests include wireless power transfer and control design.

Chunting Chris Mi (S'00–A'01–M'01–SM'03–F'12) received the B.S.E.E. and M.S.E.E. degrees in electrical engineering from Northwestern Polytechnical University, Xi'an, China, in 1985 and 1988, respectively, and the Ph.D. degree in electrical engineering from the University of Toronto, Toronto, ON, Canada, in 2001.

He was with the University of Michigan-Dearborn, Dearborn, MI, USA, from 2001 to 2015. He is currently a Professor and the Chair of electrical and computer engineering and the Director of the Department of Energy—funded Graduate Automotive Technology Education Center for Electric Drive Transportation, San Diego State University, San Diego, CA, USA. His current research interests include electric drives, power electronics, electric machines, renewable-energy systems, and electric and hybrid vehicles.